Ocean Modelling
August 2022, Volume 176, Pages 102069 (16p.)
https://doi.org/10.1016/j.ocemod.2022.102069
https://archimer.ifremer.fr/doc/00780/89206/

Archimer
https://archimer.ifremer.fr

The influence of the land-sea breeze on coastal upwelling systems: locally forced vs internal wave vertical mixing and implications for thermal fronts

Fearon Giles [1, 2, *], Herbette Steven [3], Veitch Jennifer [2, 4], Cambon Gildas [6], Vichi Marcello [1, 5]

[1] Department of Oceanography, University of Cape Town, Rondebosch, Cape Town, South Africa
[2] South African Environmental Observation Network, Egagasini Node, Cape Town, South Africa
[3] Laboratoire d'Océanographie Physique et Spatiale (LOPS), IUEM, Univ. Brest - CNRS - IRD - Ifremer, Plouzané, Brest, France
[4] Nansen-Tutu Centre, Marine Research Institute, Department of Oceanography, University of Cape Town, Rondebosch, Cape Town, South Africa
[5] Marine and Antarctic Research centre for Innovation and Sustainability (MARIS), Department of Oceanography, University of Cape Town, Rondebosch, Cape Town, South Africa
[6] Laboratoire d'Océanographie Physique et Spatiale (LOPS), IUEM, Univ. Brest - CNRS - IRD - Ifremer, Plouzané, Brest, France

* Corresponding author : Giles Fearon, email address : gfearon11@gmail.com

Abstract :

Land-sea breeze forcing near a land boundary drives both a locally forced response and an associated offshore propagating internal wave response, the effects of which can be difficult to separate. These processes enhance vertical mixing near the critical latitude for diurnal-inertial resonance (30° N/S), and are a feature of all four major eastern boundary upwelling systems. Here, we employ 1D- and 2D-vertical model configurations forced by a land-sea breeze to quantify the relative contributions of the locally forced and internal wave responses to surface currents and vertical mixing, and test sensitivity to latitude and bottom slope. We further include a sub-inertial alongshore wind to consider the role of the land-sea breeze in the context of upwelling systems. At the critical latitude, the internal waves generated via thermocline pumping near the land boundary are evanescent (in agreement with theory) and largely absent 50 km offshore. The internal waves are shown to contribute to vertical mixing, which can be 20% greater than that due to the forced response alone, further deepening the surface Ekman boundary layer. This deepening reduces the sub-inertial offshore advection of surface waters, thereby retaining the upwelling front closer to the land boundary and driving a net warming of the nearshore surface waters. Cross-shore horizontal oscillations of the upwelling front generated by the land-sea breeze drive strong diurnal variability in sea surface temperature, in agreement with observations from a cross-shore mooring array in the southern Benguela (32.3° S).

Please note that this is an author-produced PDF of an article accepted for publication following peer review. The definitive publisher-authenticated version is available on the publisher Web site.

Highlights

► Latitudinally dependent diurnal wind-driven internal waves enhance vertical mixing. ► Vertical mixing drives surface layer retention and coastal warming during upwelling. ► Diurnal wind-driven oscillations of the upwelling front explain observed temperatures. ► Bottom slope steepness controls internal wave generation at the coast.

Keywords : Land-sea breeze, Inertial oscillations, Internal waves, Vertical mixing, Critical latitude, Coastal upwelling

Please note that this is an author-produced PDF of an article accepted for publication following peer review. The definitive publisher-authenticated version is available on the publisher Web site.

1. Introduction

The land-sea breeze is a ubiquitous feature of the world's coastlines, driving diurnal wind variability which is detectable several hundred kilometres from the coast (Gille et al., 2003, 2005). At latitudes of $\phi = 30°$ N/S (referred to as the 'critical latitude' throughout this paper) the inertial frequency ($f = 2\Omega \sin \phi$) is also diurnal, giving rise to resonance between the land-sea breeze and the local inertial response of the ocean (Simpson et al., 2002; Hyder et al., 2002). As the critical latitude intersects all four of the major Eastern Boundary Upwelling Systems (EBUS), diurnal-inertial resonance is a common feature of these systems. Indeed, many documented observations of surface rotary diurnal currents in EBUS have been attributed to land-sea breeze wind forcing (Hyder et al., 2011, and references therein). The physical and biogeochemical functioning of EBUS is however largely understood in terms of the upwelling/relaxation paradigm, which responds to sub-diurnal wind variability (i.e. time-scales of longer than one day). The influence of the land-sea breeze on these systems is therefore typically assumed to be of low importance. High amplitude diurnal-inertial currents are however known to enhance shear-driven vertical mixing in coastal upwelling systems near the critical latitude, as revealed from observational evidence (Aguiar-González et al., 2011; Lucas et al., 2014) and numerical experiments (Fearon et al., 2020). Here, we build on the 1D-vertical model experiments of Fearon et al. (2020) by introducing a 2D-vertical model which includes the cross-shore dimension, allowing us to more fully explore the role of land-sea breeze forcing in the context of coastal upwelling systems near the critical latitude.

Near-inertial rotary currents are commonly excited by surface wind variability, either through an impulsive wind stress such as a storm event (e.g. D'Asaro et al., 1995), or through periodic forcing near the inertial frequency (e.g. Simpson et al., 2002). In the case of land-sea breeze forcing near the critical latitude, the surface near-inertial currents can be largely attributed to the diurnal anticyclonic rotary component of the winds (τ^{ac}), as this is the component of the forcing which rotates at the same frequency and in the same direction as the forced surface inertial oscillations (Fearon et al., 2020). Simple linearly damped slab models have been widely used to model the surface mixed layer response to wind forcing, in some cases showing reasonable agreement with observations of near-inertial rotary currents (e.g. Pollard and Millard, 1970; Pollard, 1980; Jarosz et al., 2007). The presence of a land boundary introduces a cross-shore no-flow condition at the coast which drives a barotropic response via a cross-shore surface elevation gradient. The barotropic response simultaneously dampens the wind-driven surface inertial oscillations and introduces subsurface inertial oscillations with an opposite phase to those in the surface layer (Craig, 1989; Simpson et al., 2002). Although the surface elevation gradient response behaves as an offshore propagating barotropic wave, high wave speeds ($c_0 = \sqrt{gH}$) cover typical continental shelf widths in a tiny fraction of an inertial period (Chen et al., 2017; Shearman, 2005), and as such can be interpreted as a locally forced response. Indeed, the first order cross-shore surface elevation gradient, termed the 'Craig approximation', can be applied in 1D-vertical models as a forcing term to reproduce the 180° phase shift between surface and subsurface currents (Hyder et al., 2011; Fearon et al., 2020). Throughout this paper we refer to the 'forced response' to land-sea breeze forcing near a land boundary as the superposition of the local wind-driven surface mixed layer response and the opposing first order barotropic response.

Horizontal convergences/ divergences in the locally forced near-inertial oscillations drive vertical pumping of the pycnocline, thereby initiating near-inertial internal waves which can propagate away from the generation zone (Alford et al., 2016). Near-inertial motions near coastlines are therefore a combination of the locally forced response and the offshore propagating internal wave response generated by convergence/ divergence at the land boundary (Millot and Crépon, 1981). Simple two-dimensional, linear, flat-bottom, two-layer, coastal wall models have been widely used to study the inertial response to an impulsive wind stress near the coast (e.g. Millot and Crépon, 1981; Kundu et al., 1983; Shearman, 2005; Kelly, 2019). Such models suggest

Journal Pre-proof

that the baroclinic wave generation at the land boundary plays an important role in reducing near-inertial oscillations towards the coast (Shearman, 2005). Variable bottom topography has however also been indirectly identified as a means of controlling the cross-shelf variation of near-inertial motions through its influence on the cross-shore pressure gradient (Chen and Xie, 1997). The 3D numerical experiments of Zhang et al. (2010) elucidated the latitudinal dependence of near-inertial motions, internal waves and associated diapycnal mixing in response to land-sea breeze forcing at a coast. The propagation of the internal wave energy away from the coastline is dictated by the dispersion relation for Poincare waves, which must be satisfied for propagating wave solutions to exist:

$$\omega^2 = f^2 + c_1^2 k^2 \tag{1}$$

where ω is the frequency of the waves, k is the horizontal wavenumber (considering the cross-shore dimension alone) and c_1 is the phase speed of the first baroclinic mode internal wave. Zhang et al. (2010) showed that under land-sea breeze forcing, diapycnal mixing is maximised near the critical latitude of 30° N/S, where internal wave energy is trapped at the coastline due to the low group speed of Poincare waves. Diapycnal mixing is reduced at higher and lower latitudes due to the reduction of the resonance phenomenon, while at lower latitudes energy is able to propagate offshore in the form of Poincare waves and contribute to weak diapycnal mixing outside of the forcing area.

While the forced and internal wave responses near a land boundary can be viewed as distinct processes, their similar vertical current structures and frequencies complicate the interpretation of observations and model output. Notably, the 180° phase shift between surface and subsurface near-inertial oscillations, commonly observed near land boundaries, can be easily misinterpreted as a true first baroclinic mode. This vertical current structure can however be reproduced in 1D models (Hyder et al., 2011; Fearon et al., 2020) or homogeneous models (Chen et al., 2017; Pettigrew, 1980) which exclude internal wave physics. The apparent first baroclinic mode vertical current structure is often cited as a source of shear-driven mixing, however the 1D model experiments of Fearon et al. (2020) showed that local shear-driven mixing is maximised in the absence of a land boundary, and that the introduction of the 180° phase shift between surface and subsurface layers, via the 'Craig approximation', serves to dampen shear production and diapycnal mixing. True first baroclinic mode near-inertial internal waves are however believed to play an important role in driving shear-driven turbulence and diapycnal mixing (Xing et al., 2004; Zhang et al., 2010). Separating forced and internal wave motions near a coastline has been achieved in simplified two-layer models (Kelly, 2019), or inferred through comparisons of homogenous vs stratified experiments using primitive equation models (Chen et al., 2017). The relative contribution of the forced and internal wave responses to diapycnal mixing however remains largely unstudied.

Within the context of coastal upwelling systems near the critical latitude, enhanced diapycnal mixing driven by diurnal-inertial resonance has been identified as an important mechanism for nutrient enrichment of the surface layer, with potentially significant implications for primary productivity (Aguiar-González et al., 2011; Lucas et al., 2014; Fearon et al., 2020). In addition to biological implications, the deepening of the surface mixed layer by the land-sea breeze can also influence sub-inertial processes. For instance, steepened horizontal isotherms due to land-sea breeze-driven diapycnal mixing have been identified as playing a role in enhancing sub-inertial alongshore geostrophic flows (Nam and Send, 2013). However, the implications of the land-sea breeze on sub-inertial upwelling has as far as we know not been explicitly studied.

Here, we introduce a cross-shore 2D-vertical model to study the effects of land-sea forcing on coastal upwelling systems near the critical latitude. We make use of the 1D-vertical model configuration of Fearon et al. (2020) as a proxy for the forced response, allowing us to separate the effects of the forced and internal wave responses. The 2D model is used to elucidate the effect of latitude and bottom slope on the cross-shore variability in diurnal-inertial currents, thermocline displacements and diapycnal mixing due to land-sea breeze forcing near the critical latitude. Analytically configured experiments for this purpose are set up in an analogous way to the 1D experiments described in Fearon et al. (2020), and we employ the 1D model solution as the offshore open boundary condition for the 2D model. The quantification of diapycnal mixing is aided by initialising subsurface waters with a passive tracer. We then further explore the implications of the land-sea in the context of coastal upwelling systems by considering experiments forced by the land-sea breeze alone, upwelling winds alone, and a combination of the two. We initialise subsurface waters of these experiments with lagrangian floats to track how subsurface waters are modified through land-sea breeze-driven diapycnal mixing. As in Fearon et al. (2020), we again compare a realisti-

Journal Pre-proof

cally configured model to the observations of Lucas et al. (2014), located in St Helena Bay in the Southern Benguela Upwelling System (Figure 1).

2. Methods

2.1. In-situ observations

We make use of horizontal current velocity and temperature observations from a mooring array described in Lucas et al. (2014), located in St Helena Bay in the Southern Benguela Upwelling System (Figure 1). The three fixed moorings are aligned roughly perpendicular to the local coastline, making them particularly relevant for identifying the cross-shore processes of interest in this paper. Horizontal current velocity data are obtained from bottom-mounted Acoustic Doppler Current Profilers (ADCP), while temperature data are obtained from Wirewalker wave-powered profilers (Rainville and Pinkel, 2001; Pinkel et al., 2011). Velocity and temperature data are available at a temporal frequency of 10 min and at vertical resolutions of 1 m and 0.25 m, respectively. All observations are filtered in time to provide a two hour running mean at 30 min intervals, sufficient for revealing processes at the diurnal-inertial frequency of interest. As per Fearon et al. (2020), we revisit only the 7-14 March 2011 upwelling event, having been identified as a period which clearly demonstrates the response of a highly stratified two layer system to a combination of upwelling favourable winds and strong diurnal wind variability (Lucas et al., 2014). The in-situ observations are available for download via the following Digital Object Identifiers (DOIs): Wirewalker data (`https://doi.org/10.15493/dea.mims.26052100`), ADCP data (`https://doi.org/10.15493/dea.mims.26052101`).

2.2. Ocean model

The ocean model employed in this study is the Coastal and Regional Ocean COmmunity model (CROCO) (`http://www.croco-ocean.org/`), an ocean modelling system built upon ROMS_AGRIF (Shchepetkin and McWilliams, 2005). CROCO is a free-surface, terrain-following coordinate oceanic model which solves the Navier-Stokes primitive equations by following the Boussinesq and hydrostatic approximations.

1D model experiments employ the standalone 1D version of the code described in Fearon et al. (2020), in which we retain the coast-normal horizontal pressure gradient as a forcing term computed from the 'Craig approx-

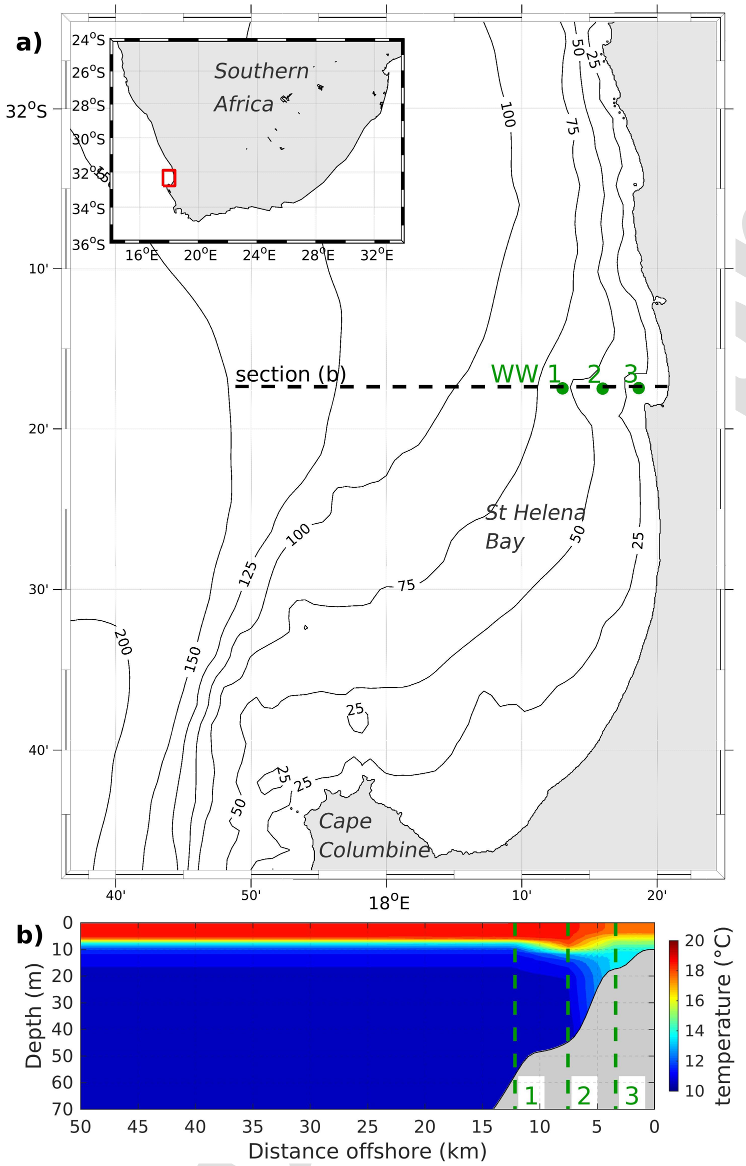

Figure 1: (a) Locality map for the Wirewalker (WW) cross-shore mooring array of Lucas et al. (2014). The black dotted line denotes the location of the section shown in (b). (b) Temperature initial condition for the realistically configured 2D model, interpolated and extrapolated from the observations on 7 March 2011. Only the closest 50 km to land boundary are shown. Bathymetry is interpolated from digital navigational charts for the region provided by the Hydrographer of the SA Navy.

Journal Pre-proof

imation'. The 1D model code can be downloaded via the following DOI: `https://doi.org/10.15493/dea.mims.26052102`.

2D model experiments are configured using the V1.0 official release of the 3D CROCO code. This is achieved by employing a shore-perpendicular grid with only 5 grid cells in the alongshore dimension (Section 2.2.1), maintaining constant alongshore bathymetry (Section 2.2.3) and making use of periodic boundary conditions along the cross-shore boundaries of the model (Section 2.2.4). Under these conditions, alongshore gradients are essentially zero and continuity dictates that divergence/ convergence of the cross-shore flow ($\frac{\partial u}{\partial x}$) must be compensated by vertical motion ($\frac{\partial w}{\partial z}$).

The parameterisation of vertical eddy viscosity and diffusivity are carried out in the present study in accordance with the k-ε turbulent closure scheme within the Generic Length Scale (GLS) formulation (Umlauf and Burchard, 2003, 2005). Implementation of the scheme within CROCO, and default settings adopted in this study, are provided in Appendix A of Fearon et al. (2020). We use an upstream-biased, dissipative horizontal advection scheme for momentum, while horizontal advection of tracers is discretized using a split and rotated third-order upstream-biased numerical scheme (Marchesiello et al., 2009). No explicit lateral viscosity is added in the model, except in sponge layers at the western open lateral boundary. As described in Fearon et al. (2020), bottom friction is parameterised using a quadratic drag law, where the bottom roughness length parameter is taken as 0.1 m. A nonlinear equation of state adapted from Jackett and Mcdougall (1995) is used for the computation of density.

Both analytically and realistically configured experiments are employed in this paper, as summarised in Table 1. The analytically configured experiments (row ID's 1 and 2 of Table 1) are designed to elucidate the processes of interest and to carry out sensitivity tests to relevant variables, while the realistically configured simulation (row ID 3 of Table 1) is compared with observations from the cross-shore mooring array of Lucas et al. (2014) over the 7-14 March 2011 upwelling event. For consistency, the 1D model configurations presented here are identical to those presented in Fearon et al. (2020), while the 2D model settings remain consistent with the 1D model settings where possible, as described below.

2.2.1. Spatial and temporal discretisation

All 2D experiments use a model domain with horizontal dimensions of 100 km (E-W) $\times$ 2.5 km (N-S), which is discretised using a regular grid of

Table 1: Summary of model experiments

ID	Description	Surface forcing	Bathymetry	Latitude
1	Diurnal-inertial resonance at a land boundary (Section 3.1)	$\tau^{ac0} = 0.03$ N m^{-2}, $\overline{\tau}_y = 0$ N m^{-2}	flat bottom	20°S, 30°S, 40°S
			1:200, 1:500	30°S
2	Diurnal-inertial resonance in the presence of upwelling (Section 3.3)	$\tau^{ac0} = 0$ or 0.03 N m^{-2}, $\overline{\tau}_y = 0$ or 0.05 N m^{-2}	1:200	30°S
3	Case study of St Helena Bay (Section 3.4)	CSAG WRF model	interpolated from navigation charts	32.3°S

500 m resolution (i.e. a 200 × 5 grid). We use 100 sigma layers to discretise the vertical dimension. A baroclinic time-step of 40 s is used to integrate the model solution over a period of 7 days from initialisation, typical of the time-scale of upwelling events. 40 barotropic time-steps are computed within each baroclinic time-step. Instantaneous model output at 30 min intervals is filtered in time to provide a two hour running mean at each time-step, consistent with the processing of observations.

2.2.2. Surface forcing

In the case of analytically configured experiments (row ID's 1 and 2 of Table 1) the land-sea breeze is approximated as a diurnal anticyclonic (anticlockwise in the southern hemisphere) rotating wind stress (τ^{ac}) of constant amplitude (τ^{ac0}), which is applied as a spatially constant forcing. Hyder et al. (2011) report diurnal anticyclonic rotary wind stress amplitudes from in-situ observations along the Namibian coastline of between 0.004 N m^{-2} and 0.051 N m^{-2}, depending on the location and observation period. Analysis of surface wind stress derived from a 3 km horizontal resolution atmospheric model indicates large spatial variability in the diurnal rotary component of winds over the Southern Benguela, with a notable enhancement over St Helena Bay (Fearon et al., 2020). In this region, the mean amplitude of the diurnal anticyclonic rotary component of the wind stress, as derived from 7 day windows over upwelling favourable months, was found to be around 0.03 N m^{-2}. We therefore adopt a value of $\tau^{ac0} = 0.03$ N m^{-2} for all analytically configured experiments presented in this paper. Time-series of the analytically configured rotary surface wind stress components ($\tau^{ac} = (\tau_x^{ac}$, τ_y^{ac})) are shown in Figure 2a.

Journal Pre-proof

Journal Pre-proof

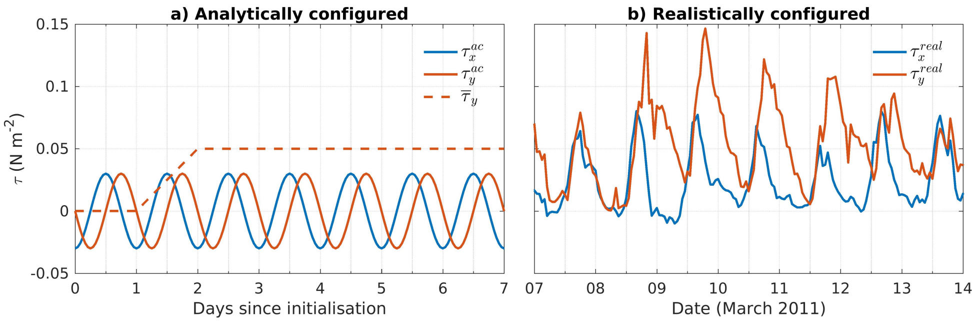

Figure 2: Time-series of surface wind stress components applied in the model configurations. (a) $\tau^{ac} = (\tau_x^{ac}, \tau_y^{ac})$ represents a diurnal anticlockwise (anticyclonic in the southern hemisphere) rotating wind stress with a constant amplitude (τ^{ac0}) of 0.03 N m^{-2}, used to represent land-sea breeze forcing. $\overline{\tau}_y$ is used to represent an upwelling favourable wind stress in the southern hemisphere. (b) Wind stress components derived from the 3 km resolution CSAG WRF atmospheric model at the outer mooring (WW1 in Figure 1) over the duration of the simulated 7-14 March 2011 upwelling event.

When upwelling is included in these experiments (row ID 2 of Table 1), it is simulated through the application of a mean alongshore wind stress ($\overline{\tau}_y$) of 0.05 N m^{-2}, being typical of the 7 day mean alongshore wind stress for St Helena Bay over upwelling favourable months (Fearon et al., 2020). $\overline{\tau}_y$ is linearly ramped up from zero to 0.05 N m^{-2} over the second day of the simulation, allowing for the preconditioning of the water column by the land-sea breeze over the first two days before the full impact of the mean alongshore wind stress is felt by the surface Ekman boundary layer. Time-series of the analytically configured surface wind stress components are shown in Figure 2a. Surface heat fluxes are excluded in analytically configured experiments.

In the case of the realistically configured experiment (row ID 3 of Table 1), bulk parameterisation is adopted for the computation of surface wind stress and surface net heat fluxes (Fairall et al., 1996, 2003) using hourly atmospheric model output from a 3 km resolution Weather Research and Forecasting (WRF) model configuration developed by the Climate Systems Analysis Group (CSAG) at the University of Cape Town (UCT). The atmospheric simulation forms part of the Wind Atlas for South Africa (WASA) project (`http://www.wasaproject.info/`) and has been validated against a number of land-based weather stations, including one deployed at the southern end of St Helena Bay over a three year period (Lennard et al., 2015).

Journal Pre-proof

Figure 2b presents time-series of surface wind stress components at the outer mooring (WW1 in Figure 1) over the duration of the simulated 7-14 March 2011 upwelling event.

2.2.3. Bathymetry and latitude

Flat bottom analytically configured experiments employ a constant water depth of 100 m depth, and we test the sensitivity of the model solution to cross-shore bottom slopes of 1:200 and 1:500 (row ID's 1 and 2 of Table 1). Flat bottom experiments are considered to be a useful reference against previous flat bottom model studies, where internal wave generation at the land boundary controls the onshore decrease in horizontal near-inertial current velocities (e.g. Shearman, 2005). Different bottom slopes allow us to test the role of the cross-shore pressure gradient (which increases with decreasing water depth according to the 'Craig approximation') in controlling the cross-shelf decrease in near-inertial motions. This mechanism was found to be a dominant driver of cross-shelf variability of near-inertial motions in the realistically configured 2D model of Chen and Xie (1997).

A maximum offshore water depth of 100 m is used for all experiments, while a minimum water depth of 20 m is employed at the land boundary. We maintain a constant alongshore bathymetry in all experiments. The realistically configured experiment (row ID 3 of Table 1) employs a nearshore bathymetry (i.e. shallower than 100 m) which is interpolated from digital versions of the most detailed available navigation charts for the region, as provided by the Hydrographer of the South African Navy (Figure 1).

Baseline experiments adopt a latitude of 30°S for testing the pure case of diurnal-inertial resonance, however we also test the model sensitivity to latitudes of 20°S and 40°S (row ID's 1 and 2 of Table 1). Latitude is expected to play a dominant role in land-sea breeze-driven near-inertial motions both through local resonance effects (Simpson et al., 2002; Hyder et al., 2002; Fearon et al., 2020) and internal wave generation Zhang et al. (2010). The realistically configured experiment adopts the realistic cross-shore mooring array latitude of $\sim$32.3°S (row ID 3 of Table 1).

2.2.4. Boundary conditions

The northern and southern boundaries are defined as periodic boundary conditions, such that all the outflows (inflows) at the southern boundary are inflows (outflows) at the northern boundary. Given the constant alongshore bathymetry, the model is effectively a 2D configuration. The eastern

Journal Pre-proof

boundary is defined as a closed land boundary, while the western boundary is applied as an open boundary condition. The open boundary requires the prescription of temperature (T), salinity (S) and velocity components (u, v). Additionally, we prescribe a passive tracer concentration boundary condition (C, in arbitrary tracer units per volume, ATU m^{-3}), used to aid the quantification of diapycnal mixing (see Section 2.3). Relaxation times of 1/4 day and 1 day are adopted for inward and outward radiation, respectively, implying strong relaxation to the specified boundary values. A sponge layer of 10 km (20 grid cells) is used to gradually ramp up the model solution in the interior of the domain to the applied boundary values within the sponge layer. The prescribed boundary conditions over each experiment are obtained from the solution of an analogously configured 1D model, integrated over the simulation period using the same initial condition and forcing as applied at the offshore extent of the 2D model.

2.2.5. Initial conditions

We remain consistent with the 1D model experiments of Fearon et al. (2020) in defining initial conditions for the 2D model experiments. Simulations are initialised from rest using a constant salinity of 35 and a temperature profile defined either analytically or from observations. In the case of analytically configured experiments (row ID's 1 and 2 of Table 1), the initial vertical profile for temperature is defined using a hyperbolic tangent function which effectively creates a two layer system with 16° C surface water overlaying 10° C subsurface water and a maximum stratification located at 10 m depth (see Fearon et al. (2020) for details). The realistic model configuration (row ID 3 of Table 1) is initialised using measured temperature profiles from the three moorings of Lucas et al. (2014) at the start of the simulation (7 March 2011). Linear interpolation is used to define the initial temperature in between the offshore and inshore moorings, while temperature data from the offshore (inshore) mooring is used to extrapolate offshore (inshore) of the moorings. While it is acknowledged that the temperature section will not be realistic at the offshore extent of the model, the intention is only to provide a stable offshore boundary so that the nearshore processes in the vicinity of the observations can be assessed. The resulting initial temperature section is shown in Figure 1b. Experiments are initialised with passive tracer concentrations of 1 and 0 ATU m^{-3} in the subsurface and surface layers, respectively.

2.3. Data analysis

As alongshore variability in the model is negligible, we only present plots and analysis of the 2D model output along a cross-shore section corresponding to the centre (i.e. third) alongshore grid cell.

We remain consistent in the computation of diapycnal mixing diagnostics as described in Fearon et al. (2020). The thermocline depth (H_s) is defined as the depth of a given isotherm, being the 11° C isotherm in the case of analytically configured experiments, and the 12.5° C isotherm in the case of the realistically configured experiment. The cumulative diapycnal mixing over each experiment is quantified through the diagnostic variable C_s, computed by integrating the passive tracer (C) over the surface layer of the model (i.e. from H_s to the surface). The depth averaged velocity vector over the surface layer of the model is used to indicate the surface layer current response in the model ($\overrightarrow{u_s} = (u_s, v_s)$). The analysis of diapycnal mixing is further aided by extracting the vertical turbulent diffusivity (K_{Tv}), as output from the k-ε turbulent closure scheme of the model. K_{Tv} is extracted at the thermocline depth as an indication of interfacial mixing in the model.

We further use the vertical displacement of the thermocline in order to diagnose internal wave generation and propagation in the model. To this end, the thermocline depth is presented as the displacement from the daily running average thermocline depth, allowing us to isolate the super-diurnal variability in the thermocline depth induced by the applied land-sea breeze forcing. Thermocline displacements are compared with the theoretical internal Rossby radius of deformation (R_d):

$$R_d = \frac{c_1}{f} \tag{2}$$

and further compared with the theoretical celerity of a long wave propagating at the interface of a two layer system:

$$c_1 = \sqrt{g' \frac{H_s H_b}{H_s + H_b}} \tag{3}$$

where $g' = \frac{\Delta\rho}{\rho} g$ is the reduced gravity acceleration. H_s and H_b are the thicknesses of the surface and bottom layers, respectively, as defined by the depth of the thermocline. g' is estimated from the temperature difference between the surface and subsurface layers and a linear expansion coefficient $\alpha = 2 \times 10^{-4}$ K^{-1}.

Journal Pre-proof

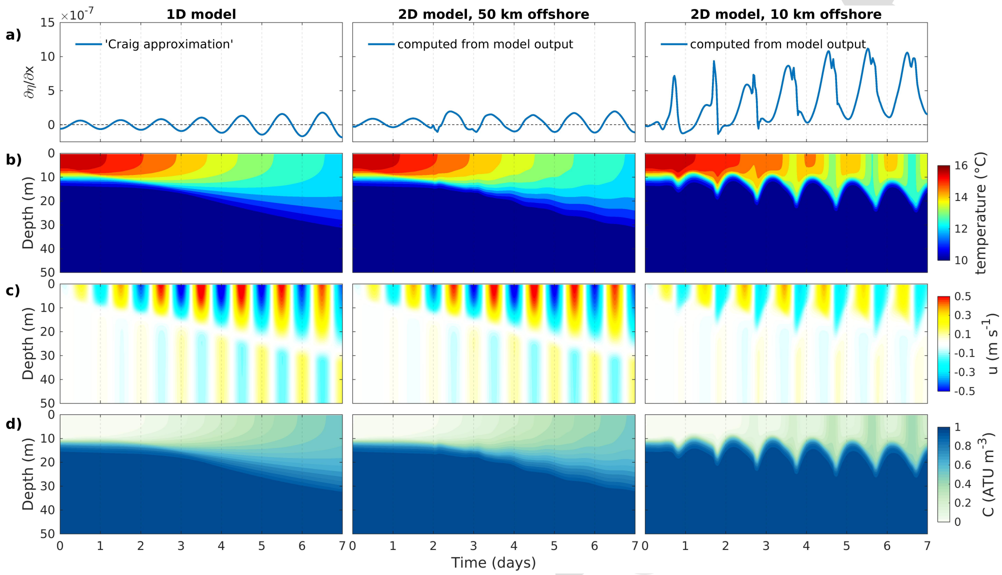

Figure 3: Flat bottom case, water depth = 100 m. Comparison of the 1D model and the 2D model at distances of 50 km and 10 km from the land boundary. Time-series of: (a) surface elevation gradient ($\frac{\partial \eta}{\partial x}$), represented by the 'Craig approximation' in the case of the 1D model, and computed from the model output in the case of the 2D model; (b) vertical profile of temperature; (c) vertical profile of cross-shore velocity (u); (d) vertical profile of passive tracer concentration (C). Results are computed from a 7 day integration of the models with input parameters τ^{ac0} = 0.03 N m^{-2}, latitude = 30° S, initial stratification (ΔT) = 6° C, initial depth of maximum stratification = 10 m.

When an upwelling favourable wind is included in the model (row ID's 2 and 3 of Table 1), the location of the upwelling front is computed from the outcropping of the diagnostic isotherm used to define the thermocline depth.

3. Results

3.1. Diurnal-inertial resonance at a land boundary

We begin by considering the response of a flat bottom 100 m deep ocean consisting of an analytically derived two-layer water column to a constant amplitude diurnal anticlockwise rotating wind stress at 30° S (the pure case of diurnal-inertial resonance). The amplitude of the applied wind stress is 0.03 N m^{-2}, and we exclude any sub-inertial upwelling from a mean alongshore wind stress. Figure 3 presents the evolution of the model output for both the 1D model configuration, as presented in Fearon et al. (2020), and

Journal Pre-proof

the 2D model configuration introduced in this paper at distances of 50 km and 10 km from the land boundary. Figure 4 presents Hovmöller diagrams for the 2D experiment showing cross-shore variability in thermocline displacements, $\log_{10} K_{Tv}$ at the depth of the 11° C isotherm (taken to represent the thermocline), and the passive tracer concentration integrated from the 11° C isotherm to the surface (C_s).

The results indicate that the 1D and 2D model solutions are almost identical at a distance of 50 km offshore. In the case of the 1D model, the cross-shore surface elevation gradient ($\frac{\partial \eta}{\partial x}$) is an applied forcing term computed from the 'Craig approximation' for the barotropic response imposed by the no-flow condition perpendicular to the land boundary, while this response is generated dynamically in the 2D model. The near-perfect agreement between the two models indicates that the reduced physics of the 1D model provides a sufficient description of the processes at this location, and therefore the enhanced shear-driven vertical mixing here is driven by the locally forced response alone. These processes are explored in detail in Fearon et al. (2020), and are therefore not elaborated further here. The excellent agreement also provides support for the methodology of using the 1D model solution as the offshore boundary condition for the 2D model. Indeed, this approach largely prevented spurious internal wave generation at the open boundary.

At a distance of 10 km offshore, the 2D model solution deviates significantly from the 1D solution, as the linear assumptions of the 'Craig approximation' are invalid. Here, in close proximity to the land boundary, horizontal gradients in cross-shore currents are high and the non-linear advection terms become important. Onshore (offshore) surface currents lead to convergence (divergence) and the downward (upward) displacement of the thermocline. The forced thermocline displacements have a diurnal periodicity, consistent with the diurnal periodicity of the wind forcing. Unlike at 50 km offshore, the results at 10 km offshore reveal diurnal variability in surface temperature and surface tracer concentrations (Figure 3b), reflecting the advection of horizontal gradients which are set up by high spatial variability in diapycnal mixing. The amplitude of the surface inertial oscillations are significantly weaker at 10 km offshore than at 50 km offshore (Figure 3c), implying reduced vertical shear and therefore reduced diapycnal mixing, as reflected in the surface tracer concentration (Figure 3d). We note that although the alongshore current velocity data are not plotted, the oscillatory nature of the currents dictates a very similar vertical structure in the alongshore currents, the only notable difference being a 6 hour phase shift when compared to the

Journal Pre-proof

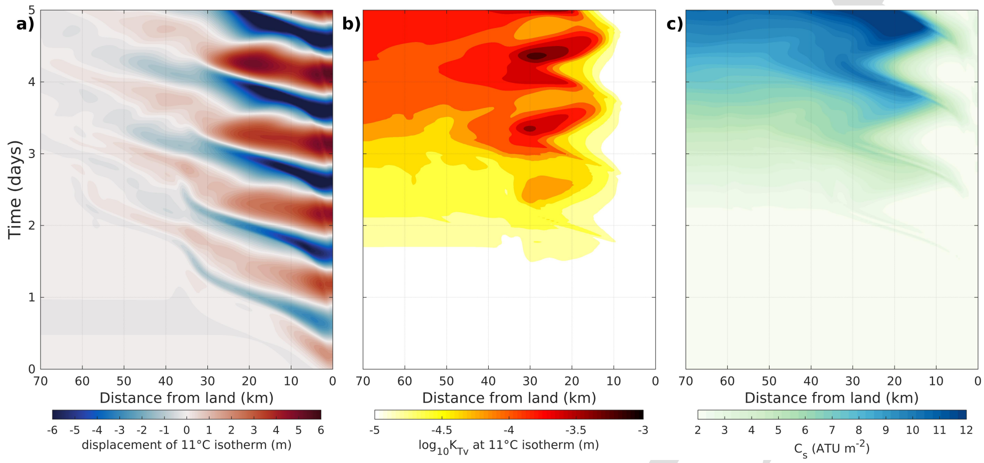

Figure 4: Hovmöller diagrams for the 2D experiment shown in Figure 3. (a) Vertical displacement of the 11° C isotherm from the daily running average isotherm depth (positive is upward); (b) $\log_{10} K_{Tv}$ at the 11° C isotherm; (c) passive tracer concentration integrated from the 11° C isotherm to the surface (C_s).

cross-shore currents.

Hovmöller diagrams of the 2D experiment (Figure 4) reveal that the vertical displacements of the thermocline propagate offshore, but are largely absent 50 km from the land boundary, indicating an evanescent internal wave response. Between 10 km and 50 km offshore, diapycnal mixing is shown to respond to a combination of the forced response and the internal wave response, generating diurnal peaks of enhanced mixing at the diagnostic thermocline (Figure 4b). The net result is an enhancement of the cumulative diapycnal mixing over and above that induced by the forced response alone, as revealed by a locally enhanced passive tracer concentration in the surface layer of the model (Figure 4c).

3.2. Sensitivity tests to latitude and bottom slope

The evanescent nature of the internal wave response to land-sea breeze forcing is governed by the latitude, as previously explored by Zhang et al. (2010), and revealed in Figure 5. Here, we contrast the simulation presented in Figures 3 and 4 (latitude = 30°S) against identical simulations run at latitudes of 20°S and 40°S. The results are presented as Hovmöller diagrams of thermocline displacement, as well as the amplitude of the surface layer velocity ($|\overrightarrow{u_s}|$) and the passive tracer concentration integrated over the surface

Journal Pre-proof

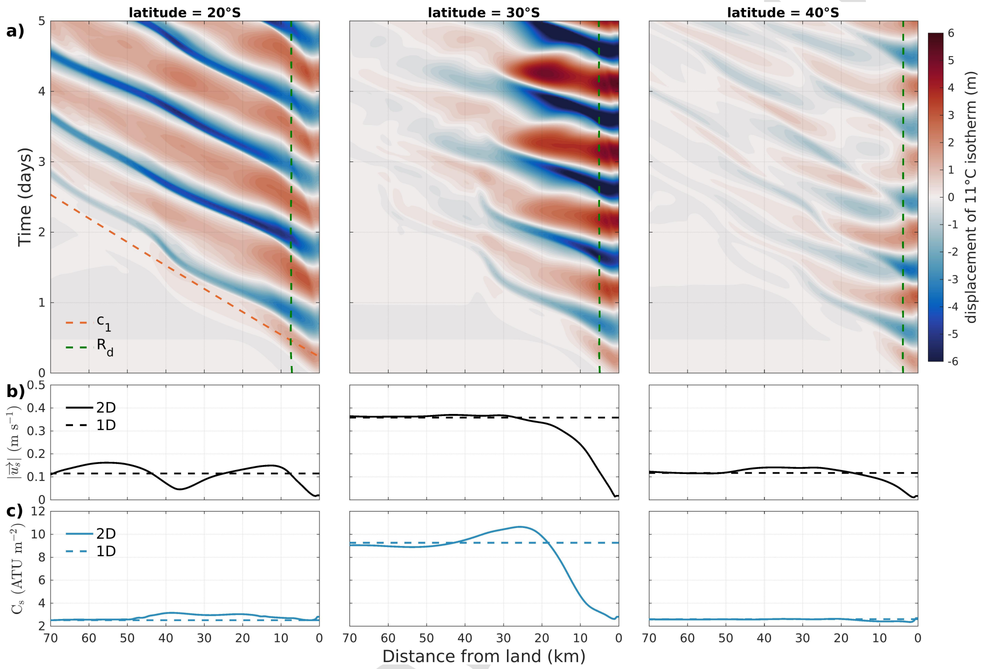

Figure 5: Flat bottom case, water depth = 100 m. Effect of latitude on cross-shore variability in thermocline displacement, current amplitude and diapycnal mixing. (a) Hovmöller diagram of the vertical displacement of the 11° C isotherm from the daily running average isotherm depth (positive is upward). The orange and green dotted lines denote the theoretical internal wave speed (c_1) and internal Rossby radius of deformation (R_d), respectively. (b) Amplitude of the surface layer velocity ($|\overrightarrow{u_s}|$), averaged over the fifth day of the simulation. (c) Passive tracer concentration integrated over the surface layer (C_s), averaged over the fifth day of the simulation. The dotted line in (b) and (c) denotes the 1D solution at the corresponding depth. Results are computed from a 7 day integration of the models with input parameters τ^{ac0} = 0.03 N m^{-2}, initial stratification (ΔT) = 6° C, initial depth of maximum stratification = 10 m.

layer (C_s), both averaged over the fifth day of each simulation. The 1D model output for $|\overrightarrow{u_s}|$ and C_s is also shown for comparative purposes, allowing us to distinguish the relative influence of the forced response (as approximated by the 1D model) and the internal waves. For consistency, $|\overrightarrow{u_s}|$ and C_s are the same metrics used to summarise the 1D model sensitivity experiments presented in Fearon et al. (2020).

The forced diurnal displacement of the thermocline is shown to occur landward of the internal Rossby radius of deformation (R_d, Equation 2), while the offshore propagation of the forced displacement is latitudinally dependent. At 20°S, the diurnal pumping of the thermocline results in offshore propagating internal waves, however these waves are evanescent at latitudes of 30°S and 40°S. Equation 1 dictates that waves can only freely propagate at latitudes where the inertial frequency f is less than the frequency of the forced diurnal displacements (i.e. equatorward of 30° N/S, such that $f < \omega$). The results indicate that the initial propagation of the internal wave away from the land boundary can be reasonably approximated by the theoretical celerity of a long wave propagating at the interface of a two layer system (c_1, Equation 3).

The amplitude of the thermocline displacement is greatest at the critical latitude of 30°S, where the amplitude of the forced surface currents and therefore convergence/ divergence at the land boundary is greatest (Figure 5b). At this latitude, the amplitude of the surface current is shown to drop off rapidly within ∼20 km of the land boundary, in good agreement with the flat bottom numerical experiments of Chen et al. (2017). Diapycnal mixing, as quantified through the passive tracer concentration integrated over the surface layer (C_s), is shown to be highest at a distance of ∼25 km offshore, and is ∼20% greater than the offshore value. As already described, the elevated mixing is attributed to the effect of the evanescent internal waves which contribute to the mixing induced by the forced response.

Both surface current amplitude and diapycnal mixing are predictably lower at latitudes of 20°S and 40°S when compared to 30°S. For the 20°S experiment the signature of the offshore propagating internal waves is evident both through deviations of the surface current amplitude (Figure 5b) and elevated diapycnal mixing (Figure 5c) when compared to the forced response. This is not seen in the 40°S experiment, where the effect of the internal wave response is negligible.

We now add an element of realism to the experiments by contrasting the 100 m water depth flat bottom configuration at 30°S already presented with

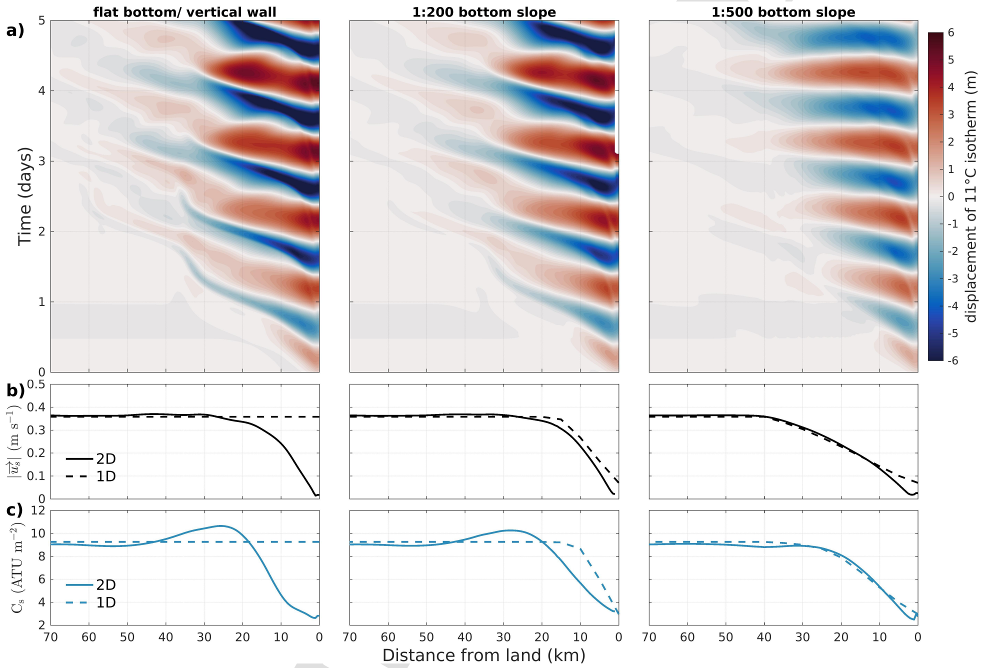

Figure 6: As per Figure 5, but testing the effect of bottom slope at a latitude of 30°S. The left panels are identical to the centre panels in Figure 5.

Journal Pre-proof

Journal Pre-proof

two experiments in which the water depth gradually increases away from the land boundary, using constant bottom slopes of 1:200 and 1:500, respectively (Figure 6). By way of comparison, the average bottom slope across the St Helena Bay mooring array is approximately 1:200 (Figure 1). The dashed lines in Figure 6b,c are taken from individual 1D model solutions run at 5 km increments from the land boundary, using the corresponding water depth of the 2D model. These 1D experiments provide insight into how a gradually reducing water depth impacts the forced response alone.

As explored in Fearon et al. (2020), the first order surface elevation gradient response serves to reduce surface oscillations and diapycnal mixing, providing a mechanism for gradually dampening the forced diurnal-inertial oscillations in shallower water depths toward the land boundary. The dampened forced response is shown to lead to a reduction in the convergence/ divergence of the forced oscillations in the surface layer, and therefore a reduction in thermocline pumping (Figure 6a). Considering the case of the 1:500 bottom slope, the 2D model results for both $|\overrightarrow{u_s}|$ and C_s are almost identical to the 1D model (right panels of Figure 6b,c), indicating that the internal wave effects on currents and diapycnal mixing are negligible. As the slope becomes steeper, so the convergence/ divergence in the forced response becomes greater and the effects of the internal waves become apparent. In these cases the 1D model over-predicts both the amplitude of the surface oscillation and diapycnal mixing within 20 km of the land boundary.

3.3. Diurnal-inertial resonance in the presence of upwelling

In the case of upwelling systems, the processes associated with diurnal-inertial resonance are embedded within Ekman dynamics driven by sub-inertial wind variability. The 2D model allows us to explore the interaction of these processes by comparing simulations forced with a land-sea breeze alone ($\tau^{ac0} = 0.03$ N m^{-2}), an upwelling wind alone ($\overline{\tau}_y = 0.05$ N m^{-2}), and a combination of the two. The values of τ^{ac0} and $\overline{\tau}_y$ are specifically chosen so that a combination of the two is representative of a 'typical' upwelling event within St Helena Bay (Section 2.2.2). We adopt a bottom slope of 1:200 for these experiments, being representative of the bottom slope within St Helena Bay (Figure 1). Figure 7 presents the temporal evolution of the modelled temperature, cross-shore currents and passive tracer for each experiment at a distance of 10 km from the land boundary.

The processes associated with the simulation forced by the land-sea breeze alone have already been shown (Figure 3), whereby diurnal variability in

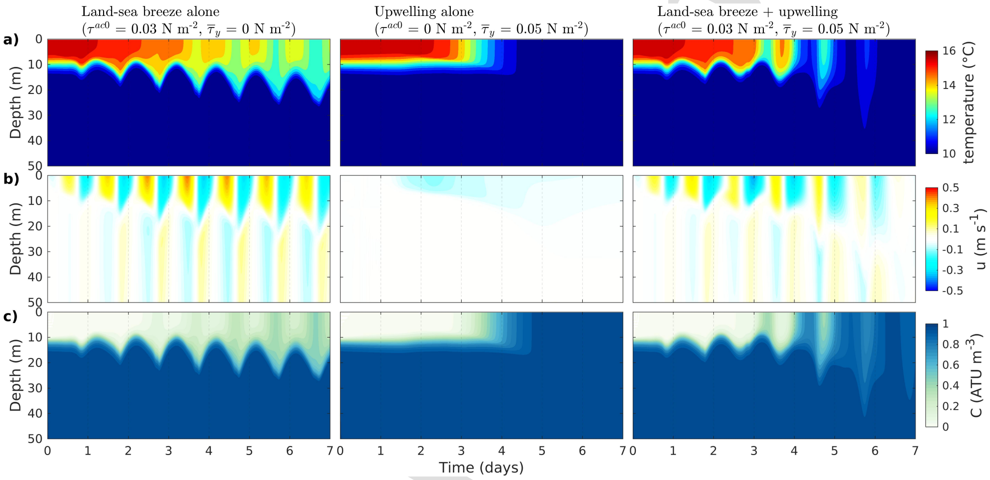

Figure 7: Effect of the land-sea breeze over a 'typical' upwelling event at a distance of 10 km from the land boundary. Simulations are forced with a land-sea breeze alone (left), an upwelling wind alone (middle), and a combination of the two (right). (a) Vertical profile of temperature; (b) vertical profile of cross-shore velocity (u); (c) vertical profile of passive tracer concentration (C). Results are computed from a 7 day integration of the 2D model with input parameters latitude = 30° S, bottom slope = 1:200, initial stratification (ΔT) = 6° C, initial depth of maximum stratification = 10 m.

Journal Pre-proof

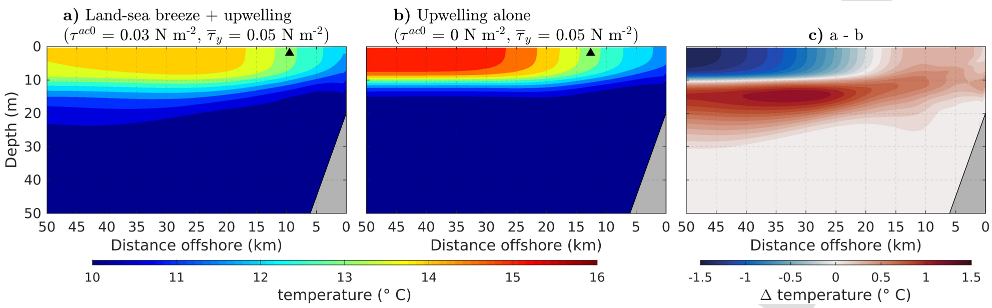

Figure 8: Modelled 7 day mean cross-shore temperature over a 'typical' upwelling event. The black triangles at the surface denote the mean location of the upwelling front, as computed from the outcropping of the 11° C isotherm. (a) Simulation forced with a combination of land-sea breeze and upwelling winds; (b) simulation forced with an upwelling wind alone; (c) difference between (a) and (b). Results are computed from a 7 day integration of the models with input parameters latitude = 30° S, bottom slope = 1:200, initial stratification (ΔT) = 6° C, initial depth of maximum stratification = 10 m.

surface temperature is driven by a combination of high spatial variability in diapycnal mixing and advection due to the surface inertial oscillations. The simulation forced by the upwelling wind alone shows considerably reduced diapycnal mixing, and shows the offshore transport of the surface layer in response to the sustained alongshore wind stress (centre panel of Figure 7b). The combined effect of land-sea breeze and upwelling winds generates super-diurnal advection of the upwelling front, leading to pronounced diurnal variability in surface temperatures. The inertial oscillations (left panels of Figure 7) are superimposed onto the sub-inertial transport (centre panels of Figure 7), resulting in the repeated cross-shore back and forth advection of strong horizontal temperature gradients past the shown output location (right panels of Figure 7). Large diurnal variability in temperature will persist provided the location of interest is within one oscillation radius of the steep horizontal temperature gradients associated with the upwelling front (an oscillation velocity of 0.5 m s^{-1} at 30° S has an oscillation radius ($\frac{u}{f}$) of 6.9 km). This phenomenon is invoked in the interpretation of the results of the realistically configured experiment, as described in Section 3.4.

In addition to the super-diurnal advection of the upwelling front, the inclusion of the land-sea breeze is shown to significantly influence the mean cross-shore temperature over the modelled upwelling event (Figure 8). The mean location of the upwelling front is also shown, as computed from the

Journal Pre-proof

outcropping of the 11° C isotherm. At the offshore extent of the shown section (i.e. outside the influence of the upwelling front), the applied diurnal wind variability is shown to result in a significant cooling of the surface, which overlays a commensurate warming. Despite the surface cooling due to diapycnal mixing, the results indicate a net warming of mean surface waters within ∼20 km of the coast due to the inclusion of land-sea breeze forcing, relative to the case with upwelling winds alone. We posit two explanations for this perhaps unintuitive result.

Firstly, although the Ekman transport ($M_E = \frac{\overline{\tau}_y}{\rho f}$) is the same in both cases, the cross-shore velocity of the surface Ekman boundary layer ($U_E = \frac{M_E}{H_s}$) is reduced when the land-sea breeze is included, due to diapycnal mixing-induced deepening of the surface layer (H_s). This leads to a persistently landward location of the upwelling front when land-sea breeze forcing is applied, effectively resulting in retention of surface waters and a net warming in the nearshore (this concept is further discussed in Section 4).

The second potential explanation for the nearshore warming due to the inclusion of diurnal wind variability is that the enhanced diapycnal mixing leads to a warming of subsurface waters, which are carried by the upwelling circulation toward the inshore and surface. As it is not immediately apparent which of these two processes (the location of the upwelling front vs modified upwelled water) is of leading order in explaining the nearshore surface warming, Appendix A presents diagnostics designed to reveal the relative contribution of each. The analysis suggests that the nearshore warming due to the inclusion of the land-sea breeze is primarily driven by the location of the upwelling front, while the upwelling of warmer waters due to enhanced vertical mixing plays a secondary role.

3.4. Case study of St Helena Bay

We now present the final more comprehensive experiment, being a realistically configured simulation for comparison with the nearshore observations of Lucas et al. (2014). The model solution is integrated over a 7 day period, starting on 7 March 2011 from the temperature section shown in Figure 1, and forced with hourly winds and heat fluxes derived from the 3 km resolution CSAG WRF model output.

Figure 9 compares the observed and modelled temperature across the mooring array, including summary statistics of model bias, centred root mean square difference (RMSD) and Pearson's correlation coefficient, as a function of depth. The model is shown to reproduce the salient features of the

Journal Pre-proof

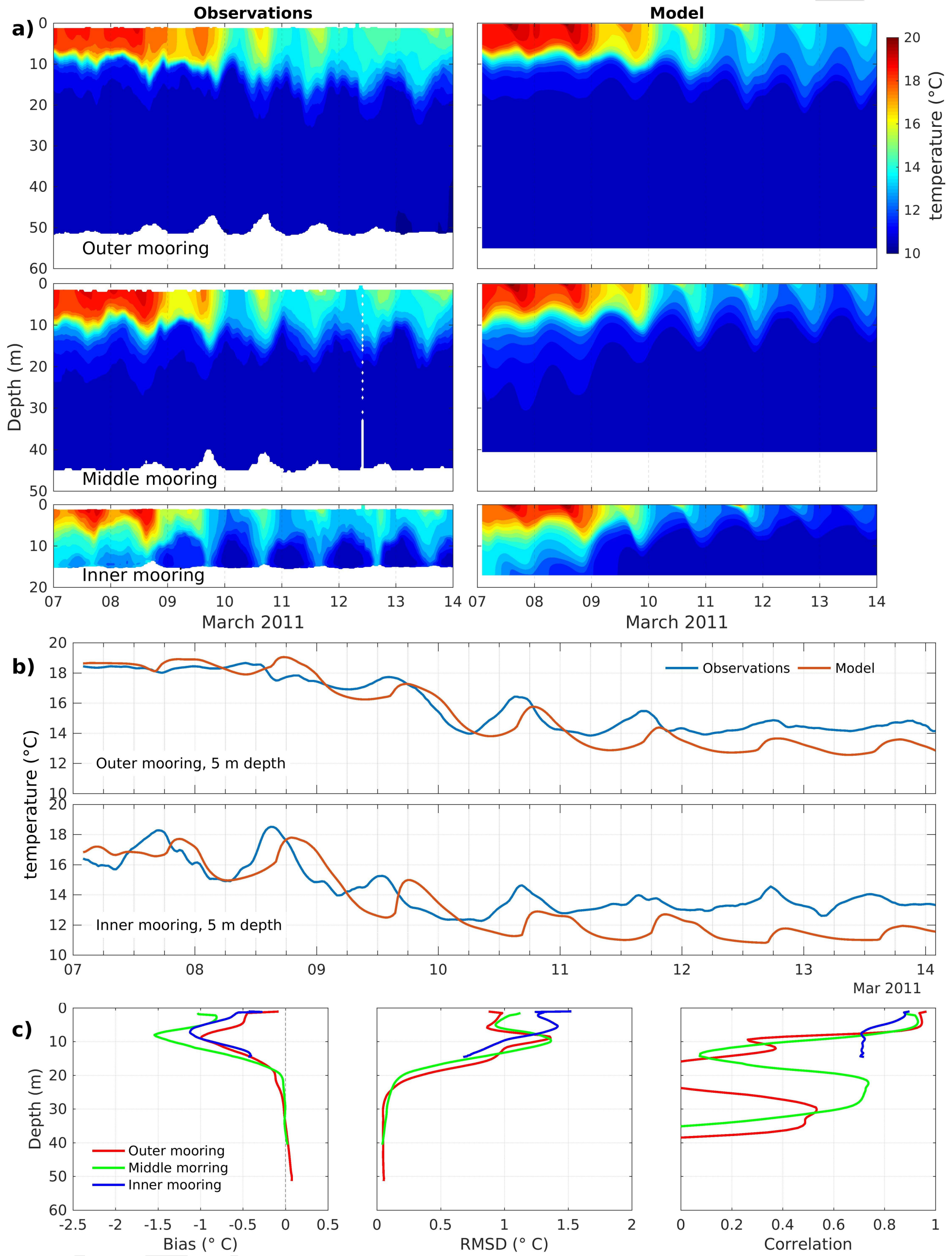

Figure 9: Observed and modelled temperature over an upwelling event accompanied by land-sea breeze forcing from a mooring array in St Helena Bay (Figure 1). (a) Temporal evolution of the observed (left) and modelled (right) temperature profile at the outer (∼12.7 km offshore), middle (∼8.1 km offshore) and inner (∼3.9 km offshore) moorings; (b) time-series of observed and modelled temperature at the outer and inner moorings at 5 m depth; (c) summary statistics for modelled temperature as a function of depth. The model is shown to reproduce the salient features of the temperature observations, characterised by diurnal-inertial variability in surface temperature, large thermocline displacements and a net cooling of surface waters.

temperature observations at all three moorings, which are characterised by significant diurnal-inertial variability in surface temperature and a net cooling of surface waters over the considered period. The analytically configured 2D experiments have highlighted the mechanism whereby near the critical latitude of 30° S, diurnal-inertial oscillations in the presence of sub-inertial upwelling produces strong diurnal variability in surface temperature through repeated advection of strong horizontal temperature gradients over the measurement location. The pumping of the thermocline, characteristic of the internal wave response as revealed in the analytically configured 2D experiments, is also evident in both the observations and the model. It is expected that the 2D model would tend to over-estimate thermocline displacements, as the divergence/ convergence of the cross-shore flow ($\frac{\partial u}{\partial x}$) is compensated by vertical motion ($\frac{\partial w}{\partial z}$) alone due to the exclusion of alongshore gradients ($\frac{\partial v}{\partial y}$) in the model. Alongshore velocity gradients however appeared to have played a minor role over the observation period, as revealed by similar amplitude ($\sim$5 m) thermocline displacements in the both model and the observations.

The model performance is best at the surface, as reflected by high correlation coefficients at all three moorings (>0.8 for depths shallower than $\sim$5 m, Figure 9c). The significant reduction in temperature correlation near the base of the thermocline can in part be explained by an over-prediction in sub-inertial upwelling and the consequent over-prediction in thermocline lifting, as reflected in a negative near-surface temperature bias across the mooring array (left panel of Figure 9c). This could be attributed to an over-prediction in the mean alongshore surface wind stress derived from the CSAG WRF model, or potentially due to the advection of alongshore variability in temperature which is explicitly excluded in the model. The low (even negative) correlations in the subsurface water (>20 m depth) at the middle and outer moorings are attributed to the lack of a meaningful temperature signal here over the considered event, as evidenced by the low RMSD in this region of the water column.

The time-series comparisons at 5 m depth (Figure 9b) indicate a phase lag ($\sim$6 hrs) in the timing of the diurnal fluctuations in near-surface temperature, which may reflect shortcomings in the timing of the land-sea breeze in the CSAG WRF model forcing. One potential explanation for this could be due to shortcomings in the sea surface temperature (SST) input to the CSAG WRF model. Upwelling is known to impact the timing of the land-sea breeze (Seroka et al., 2018), while the WRF model uses daily SST fields derived from satellite observations which contain systematic errors in upwelling regions

Journal Pre-proof

(Meneghesso et al., 2020) and do not capture super-diurnal variability in SST's.

The observed and modelled cross-shore component of velocity for the outer and inner moorings are compared in Figure 10 (ADCP data from the middle mooring were mostly missing over this period and is therefore not shown). While the salient features of the vertical structure of the currents are reproduced in the model, the time-series comparisons (Figure 10b) again reveal phase differences in the diurnal-inertial oscillations, where the model lags the observations by ∼6 hrs at both the outer and inner moorings.

Despite the presence of the time lag, correlation coefficients at the outer mooring are between ∼0.4 and ∼0.6 for the subsurface currents, while a maximum of ∼0.7 is attained for the near-surface currents (Figure 10c). The model correlation coefficients drop to negative values in the region of the thermocline, where the 180° phase shift between the surface and subsurface currents is observed. Poor correlation in this region is not surprising, as any misrepresentation in the depth of the 180° phase shift will have a notable impact on the correlations in this region of the water column. Current correlations are lower at the inner mooring (between ∼0.2 and ∼0.4), where the amplitude of the diurnal-inertial signal is weaker. The modelled currents at this mooring appear to be hampered by the signature of an over-prediction in sub-inertial upwelling circulation, as evidenced by negative (positive) cross-shore current biases in the surface (subsurface) (Figure 10c). These biases are in agreement with the cool surface temperature bias visible in Figure 9.

4. Discussion and conclusions

In this paper we have employed novel 2D model experiments to gain insight into the cross-shore processes governing the response of coastal upwelling systems to land-sea breeze forcing. In addition to testing model sensitivity to relevant variables in analytically configured experiments, a realistically configured experiment has been compared with three nearshore moorings orientated perpendicular to the local coastline in St Helena Bay, located in the Southern Benguela Upwelling System (Lucas et al., 2014). Our analytically configured experiments have focussed on the response of upwelling systems at the critical latitude of 30° N/S, where the diurnal periodicity of the land-sea breeze is resonant with the inertial frequency and the locally forced response is maximised (Craig, 1989; Simpson et al., 2002; Fearon et al., 2020). Given the mooring array latitude of 32.3° S, the observa-

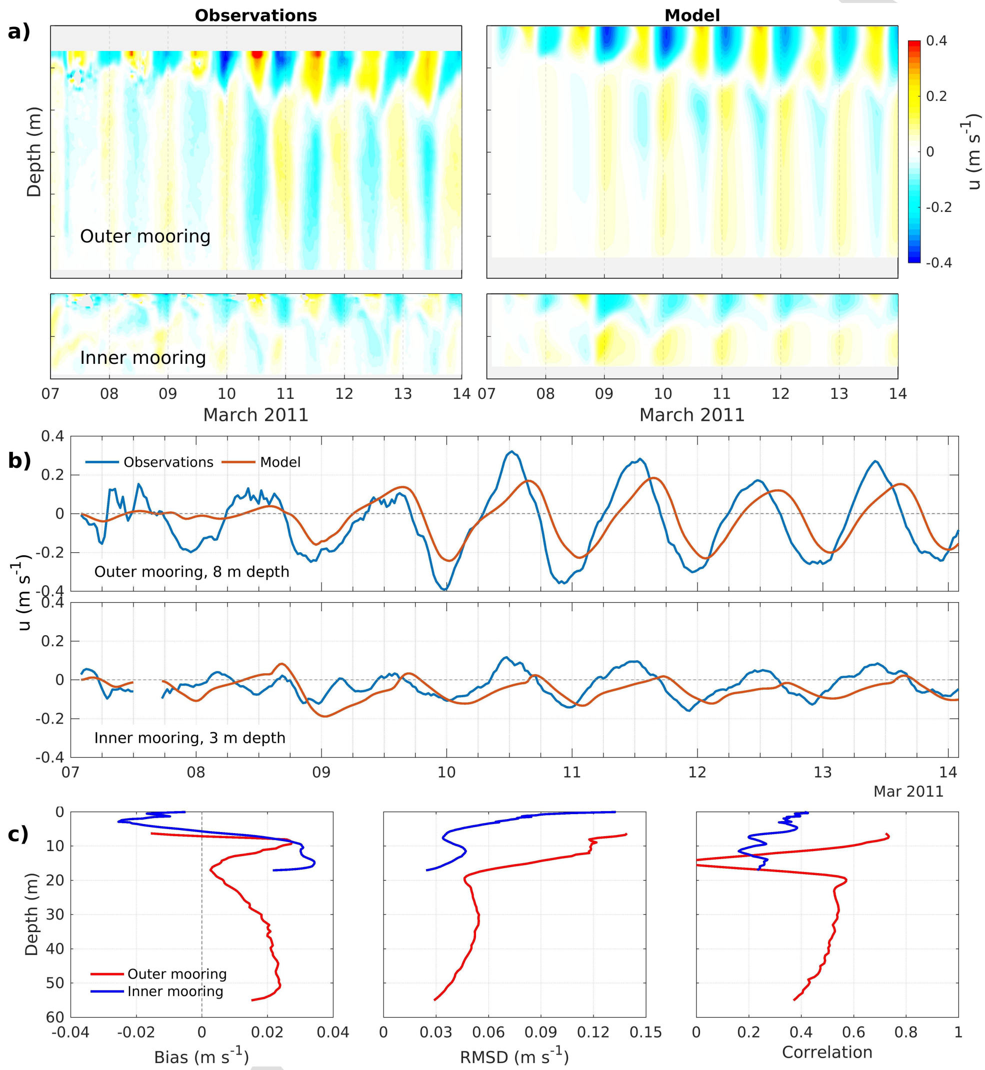

Figure 10: Observed and modelled cross-shore velocity (u) over an upwelling event accompanied by land-sea breeze forcing from a mooring array in St Helena Bay (Figure 1). (a) Temporal evolution of the observed (left) and modelled (right) cross-shore velocity profile at the outer (~12.7 km offshore) and inner (~3.9 km offshore) moorings; (b) time-series of observed and modelled cross-shore velocity at the outer and inner moorings at 8 m and 3 m depths, respectively; (c) summary statistics for modelled cross-shore velocity as a function of depth. ADCP data from the middle mooring were mostly missing over this period and is therefore not shown. The model is shown to reproduce the salient features of the current observations, characterised by diurnal-inertial oscillations in surface and subsurface layers with a 180° phase shift between the two.

Journal Pre-proof

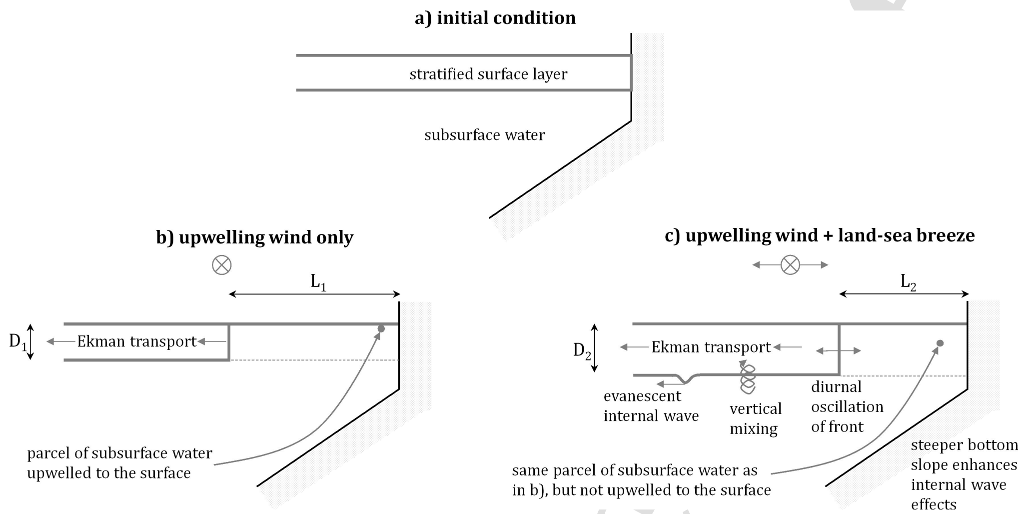

Figure 11: Summary of key processes resulting from land-sea breeze forcing in upwelling systems near the critical latitude of 30° N/S.

tions provide a particularly relevant ground truth for the presented 2D model configuration. Notwithstanding model shortcomings which include an over-prediction in sub-inertial upwelling and notable phase lags in the modelled diurnal-inertial response, the favourable comparison with the observations provides some confidence in the dynamics elucidated by the analytically configured experiments.

The presented results are relevant for all regions under the influence of land-sea breeze forcing near the critical latitude, which includes all four of the major Eastern Boundary Upwelling Systems (EBUS). The relevance of the results naturally diminishes away from the critical latitude, where the locally forced resonance phenomenon becomes weaker (e.g. Figure 5 and Figure 10 of Fearon et al., 2020). Hyder et al. (2011) argue the region of influence to lie between latitudes of 23° and 40° N/S. The key processes elucidated by the experiments presented in this paper are summarised in Figure 11 and discussed below.

4.1. Separation of the forced and internal wave responses

Contrasting results from the 2D model with those of the 1D model presented in Fearon et al. (2020) has allowed us, for the first time, to identify the respective roles of the locally forced response (as approximated by the 1D model) and the internal wave response to land-sea breeze forcing near the critical latitude. While the focus of this paper is on coastal upwelling systems, the findings of these purely land-sea breeze forced experiments would apply to any two layer coastal systems near the critical latitude.

As the locally forced response to the land-sea breeze is maximised at the critical latitude of 30° N/S, here we also find the maximum amplitude thermocline displacements due to convergence/ divergence of the forced oscillations at the land boundary. Although the internal waves are evanescent at the critical latitude, in agreement with theory and the numerical experiments of Zhang et al. (2010), they provide an additional source of shear-driven diapycnal mixing. In the considered configuration, the effect is maximised at a distance of $\sim$25 km from the wave generation zone at the land boundary, where diapycnal mixing can be $\sim$20% greater than that due to the forced response alone. The influence of the internal waves extends to $\sim$50 km from the land boundary, offshore of which the 1D and 2D model solutions are in near-perfect agreement.

Sensitivity tests have revealed the importance of the bottom slope in governing the processes driving the cross-shore variability in near-inertial motions. The steepness of the bottom slope determines the rate at which the locally forced oscillations are dampened toward the coast, thereby influencing the convergence/ divergence of the surface currents and thermocline pumping. Internal wave generation at the coast is therefore dampened by a gradually sloping bottom. This is in agreement with previous 2D primitive equation experiments over the gradually sloping Texas-Louisiana shelf, where non-linear advection terms were of secondary importance and the first order cross-shore surface elevation gradient was found to play a dominant role in the cross-shore variability in near-inertial oscillations (Chen and Xie, 1997). In contrast, a simple two-layer coastal wall model has been used to identify the internal wave generation at the boundary as the driving mechanism for explaining the drop-off in near-inertial energy toward the coast (Shearman, 2005). Our sensitivity experiments serve to reveal how the bottom slope governs which of these processes (first order surface elevation gradient vs internal wave generation) dominate the reduction in near-inertial motions toward the coast. Steeper bottom slopes are required to enhance the internal wave response and allow for elevated diapycnal mixing over and above what would be expected from the forced response alone.

4.2. The influence of the land-sea breeze on sub-inertial upwelling

The inclusion of a sub-inertial alongshore wind stress in the 2D model experiments has allowed for further reflection on the role of diurnal-inertial resonance within the context of sub-inertial upwelling dynamics. Our results reveal how the combined effect of sub-inertial upwelling and inertial oscillations can produce pronounced diurnal variability in nearshore surface temperatures, driven by horizontal diurnal advection of strong cross-shore temperature gradients, which are ever-present in upwelling systems. Local land-sea breeze forcing has been identified as playing a key role in diurnal temperature variability in a number of in-situ observations in EBUS (Kaplan et al., 2003; Woodson et al., 2007; Bonicelli et al., 2014; Walter et al., 2017) and is evident in the nearshore observations of Lucas et al. (2014) (Figure 9). The 2D model experiments presented here clearly demonstrate a driving mechanism of this phenomenon, although it is noted that solar irradiance is an additional mechanism which would further contribute to diurnal variability in sea surface temperatures. While not explicitly considered in this paper, the impact of solar irradiance on surface temperatures over the presented observation period can be inferred from the 1D model results at the outer mooring (Figure 6 of Fearon et al., 2020), which included realistic surface heat fluxes. Comparison of the modelled temperature at the outer mooring from the 2D model (Figure 9a) with that of the 1D model suggests that the advection of horizontal gradients was the dominant mechanism in driving the diurnal sea surface temperature variability over the considered observation period.

Our simulations have further highlighted how deepening of the thermocline due to diurnal-inertial resonance near the critical latitude can lead to a reduction in sub-inertial offshore advection of the surface Ekman boundary layer, as illustrated in Figure 11. As offshore Ekman transport is the same in both Figure 11b and Figure 11c, volume conservation dictates that $D_1L_1 = D_2L_2$, and therefore the landward offset of the upwelling front will scale linearly with the increased depth in the surface Ekman boundary layer. For example, if a mean alongshore wind drives a 15 m deep Ekman boundary layer 10 km offshore, the same wind will drive a 20 m deep Ekman boundary layer 7.5 km offshore ($15 \div 20 \times 10$). Shallower surface mixed layers elicit higher amplitude oscillations in the surface layer and greater mixing (Fearon et al., 2020), implying that regions prone to the development of shallow surface layers, such as retention zones in the lee of capes (e.g. Graham and Largier, 1997; Oliveira et al., 2009), are likely to be most affected by this pro-

Journal Pre-proof

cess. Advective losses during active upwelling can contribute to a reduction in productivity within upwelling systems, while the retention of upwelled waters is important for the accumulation of high biomass coastal blooms (Pitcher et al., 2010). Our results imply that the land-sea breeze may play a contributing role in surface water retention in these areas through reduced offshore advection of the surface layer during upwelling events.

The retention of surface waters due to the inclusion of land-sea breeze forcing has been shown to drive a net warming of nearshore surface waters, primarily due to the landward displacement of the upwelling front, while modification of subsurface waters through enhanced diapycnal mixing plays a secondary role. Offshore of the influence of the upwelling front, surface waters are cooled through the entrainment of subsurface waters via diapycnal mixing. These results suggest that the misrepresentation of the land-sea breeze in global and regional models of EBUS may contribute to nearshore temperature biases in these models. Such biases are largely attributed to errors in the representation of the low frequency alongshore wind stress in the atmospheric forcing products (e.g. Richter, 2015; Small et al., 2015), while the influence of the land-sea breeze is over-looked as a potential source of systematic error. Our results suggest that the improvement in the spatial and temporal representation of the land-sea breeze could be important in alleviating this source of systematic bias, particularly near the critical latitude and in areas susceptible to the development of shallow surface mixed layers.

We note that our results have been limited to short duration (7 day) experiments with a simplified 2D model. While these experiments have been useful to elucidate event-scale dynamics, further work is required to assess the overall role of these processes within EBUS, where Ekman dynamics are also counteracted by eddy effects (Thomsen et al., 2021). Inter-annual simulations of realistically configured 3D models of EBUS, which both include and exclude land-sea breeze forcing, are expected to provide useful insights to this end. Such regional simulations are typically forced at the surface by an atmospheric model which is itself forced by sea surface temperatures which do not capture land-sea breeze effects on the upwelling front. This shortcoming was invoked as a possible source of the phase lag error in the realistically configured simulation (Section 3.4). Previous studies have identified coastal upwelling as influencing the land-sea breeze both through an earlier onset and enhanced intensity (Clancy et al., 1979; Seroka et al., 2018), which may in turn have a positive feedback on upwelling favourable winds (Franchito et al., 1998). This paper has further explored how the land-sea breeze may impact

Journal Pre-proof

the location of the upwelling front near the critical latitude; processes which themselves appear likely to influence the land-sea breeze. It is suggested that two-way coupled ocean-atmosphere experiments may prove to be particularly insightful in exploring this two-way feedback near the critical latitude.

4.3. Improved understanding of the St Helena Bay observations

The results of this paper provide an opportunity for further reflection on the processes governing the nearshore observations of Lucas et al. (2014). While the forced response, as approximated by the 1D model, reproduces many of the salient features of the observations at the offshore mooring (Figure 6 of Fearon et al., 2020), the 1D model was shown to over-predict the deepening of the thermocline through diapycnal mixing, under-predict net cooling of surface waters and lack sufficient diurnal-inertial variability in both surface temperature and vertical displacement of the thermocline. The realistically configured 2D model has significantly alleviated these shortcomings (Figures 9 and 10), suggesting that the analytically configured 2D experiments may be useful in interpreting the observations. Figure 6 confirms that for a 1:200 bottom slope (the approximate slope across the mooring array) and an offshore distance of just $\sim$12.7 km, an over-prediction in the amplitude of the surface oscillation and consequent deepening of the thermocline is to be expected in the 1D model. Here, the 2D model experiments reveal the $\sim$5 m amplitude thermocline displacements to be the signature of internal waves generated at the land boundary. The inclusion of sub-inertial upwelling circulation in the 2D model alleviates the 1D model shortcomings of an under-prediction of net cooling of surface waters (although upwelling is over-predicted in the 2D model), and provides the mechanism for generating the observed diurnal variability in surface temperatures, as already discussed.

Lucas et al. (2014) identified vertical mixing-driven nutrient flux to be of high importance in governing observed phytoplankton growth across the mooring array. While the 2D model confirms shear-induced diapycnal mixing to be a feature over the mooring array, an important consequence of the presented experiments is that the region of maximum diapycnal mixing is in fact expected to be located offshore of the observations. It therefore seems plausible that the effect of the land-sea breeze on the phytoplankton response may well have been further enhanced offshore of the the mooring array. This suggests that our understanding of event-scale phytoplankton dynamics in the region would greatly benefit from high-frequency observations of the water column which extend across the full width of St Helena

Journal Pre-proof

Journal Pre-proof

Bay.

Acknowledgements

The financial assistance of the South African Environmental Observation Network (SAEON) towards this research is acknowledged. Opinions expressed and conclusions arrived at are those of the author(s) and are not necessarily to be attributed to SEAON. GF further acknowledges grants from LabexMER and the French Embassy in South Africa which greatly facilitated this research. GF and MV received funding from an anonymous donor as part of the Whales and Climate Research Program (https://www.whalesandclimate.org/), as well as from the European Union's Horizon 2020 research and innovation programme under grant agreement No 862923. We thank the Climate Systems Analysis Group (CSAG) for the provision of their WRF atmospheric model output and the South African Navy Hydrographic Office (SANHO) for the provision of bathymetric data. The study benefitted from computational facilities provided by the University of Cape Town's ICTS High Performance Computing team (hpc.uct.ac.za).

Appendix A. Diagnostics explaining warming of nearshore surface waters in response to land-sea breeze forcing

Figure 8 indicates nearshore surface warming due to the inclusion of land-sea breeze forcing, while two processes are identified as possible drivers of this result:

1. the landward location of the upwelling front due to a deepened Ekman boundary layer and
2. the warming of subsurface water through diapycnal mixing, which is then upwelled to the surface.

In this appendix we present diagnostics designed to reveal which of these two processes is of leading order in explaining the nearshore surface warming.

The contribution of the location of the upwelling front (blue line in Figure A.12b) is computed as follows: the cross-shore temperature profile from the surface layer of the simulation forced by an upwelling wind alone is extracted at each 30 min time-step; a landward offset to this profile is then applied according to the difference in the upwelling front locations shown in Figure A.12a; the difference between the original and the offset cross-shore

Journal Pre-proof

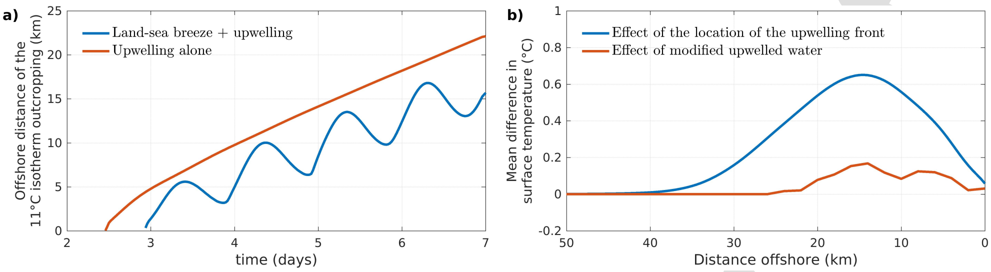

Figure A.12: Diagnostics used to explain the warming of nearshore surface waters in response to the inclusion of the land-sea breeze, as shown in Figure 8. (a) Time-series of the offshore distance of the 11° C isotherm in the surface layer of the model (used as a proxy for the upwelling front) for the simulations shown in Figure 8. (b) Estimates of the relative contribution of the two processes (the location of the upwelling front vs modified upwelled water) which explain the warming of nearshore waters due to the inclusion of the land-sea breeze.

temperature profiles is then computed. The effect shown in Figure A.12b is the mean temperature difference over the entire 7 day simulation.

The contribution of the upwelling of warmer subsurface waters is computed through the use of CROCO's online Lagrangian floats module. Both simulations (i.e. excluding and including land-sea breeze forcing) are initialised with neutrally buoyant Lagrangian floats from the depth of the 11° C isotherm to the bottom in vertical increments of 1 m and horizontal increments of 500 m (the horizontal grid resolution), thereby covering subsurface waters over the entire model domain. The temperature at the location of the floats, as interpolated from the Eulerian model, is saved at 30 min intervals over each simulation. Temperature differences between the Eulerian model at the location of the Lagrangian floats and the initial temperature of Lagrangian floats are used to quantify how subsurface water is modified by land-sea breeze-driven diapycnal mixing over the upwelling simulations. The red line in Figure A.12b) is computed as follows: all Lagrangian floats in the upper 5 m of the water column are identified at each 30 min time-step and taken to represent upwelled water; the difference between the temperature of the Eulerian field at the location of the floats and the original temperature of the floats is computed (quantifying how the upwelled water has been modified through diapycnal mixing); the offshore distance of the floats are used to construct a cross-shore profile of the surface temperature difference, using 2 m bins in the cross-shore direction and averaging the temperature difference from all 'upwelled' Lagrangian floats contained within each 2 m bin.

Journal Pre-proof

The effect shown in Figure A.12b is the mean temperature difference over the entire 7 day simulation forced by a combination of land-sea breeze and upwelling winds, over and above that computed from the simulation forced by an upwelling wind alone. This approach is designed to capture how the temperature of subsurface water has been modified by enhanced diapycnal mixing offshore of the upwelling front, prior to upwelling.

Figure A.12b suggests that the nearshore warming due to the inclusion of the land-sea breeze is primarily driven by the location of the upwelling front, while the upwelling of warmer waters due to enhanced vertical mixing plays a secondary role.

References

Aguiar-González, B., Rodríguez-Santana, Á., Cisneros-Aguirre, J., Martínez-Marrero, A., 2011. Diurnal–inertial motions and diapycnal mixing on the Portuguese shelf. Continental Shelf Research 31, 1193–1201. doi:10.1016/j.csr.2011.04.015.

Alford, M.H., MacKinnon, J.A., Simmons, H.L., Nash, J.D., 2016. Near-Inertial Internal Gravity Waves in the Ocean. Annual Review of Marine Science 8, 95–123. doi:10.1146/annurev-marine-010814-015746.

Bonicelli, J., Moffat, C., Navarrete, S.A., Largier, J.L., Tapia, F.J., 2014. Spatial differences in thermal structure and variability within a small bay: Interplay of diurnal winds and tides. Continental Shelf Research 88, 72–80. doi:10.1016/j.csr.2014.07.009.

Chen, C., Xie, L., 1997. A numerical study of wind-induced, near-inertial oscillations over the Texas-Louisiana shelf. Journal of Geophysical Research: Oceans 102, 15583–15593. doi:10.1029/97JC00228.

Chen, S., Chen, D., Xing, J., 2017. A study on some basic features of inertial oscillations and near-inertial internal waves. Ocean Science 13, 829–836. doi:10.5194/os-13-829-2017.

Clancy, R.M., Thompson, J.D., Hurlburt, H.E., Lee, J.D., 1979. A Model of Mesoscale Air-Sea Interaction in a Sea Breeze-Coastal Upwelling Regime. Monthly Weather Review 107, 1476–1505. doi:10.1175/1520-0493(1979)107<1476:AMOMAS>2.0.CO;2.

Journal Pre-proof

Craig, P.D., 1989. A model of diurnally forced vertical current structure near 30° latitude. Continental Shelf Research 9, 965–980. doi:10.1016/0278-4343(89)90002-2.

D'Asaro, E.A., Eriksen, C.C., Levine, M.D., paulson, C.A., Niiler, P., Van Meurs, P., 1995. Upper-Ocean Inertial Currents Forced by a Strong Storm. Part I: Data and Comparisons with Linear Theory. Journal of Physical Oceanography 25, 2909–2936. doi:10.1175/1520-0485(1995)025<2909:UOICFB>2.0.CO;2.

Fairall, C.W., Bradley, E.F., Hare, J.E., Grachev, A.A., Edson, J.B., 2003. Bulk Parameterization of Air–Sea Fluxes: Updates and Verification for the COARE Algorithm. Journal of Climate 16, 571–591. doi:10.1175/1520-0442(2003)016<0571:BPOASF>2.0.CO;2.

Fairall, C.W., Bradley, E.F., Rogers, D.P., Edson, J.B., Young, G.S., 1996. Bulk parameterization of air-sea fluxes for Tropical Ocean-Global Atmosphere Coupled-Ocean Atmosphere Response Experiment. Journal of Geophysical Research: Oceans 101, 3747–3764. doi:10.1029/95JC03205.

Fearon, G., Herbette, S., Veitch, J., Cambon, G., Lucas, A.J., Lemarié, F., Vichi, M., 2020. Enhanced Vertical Mixing in Coastal Upwelling Systems Driven by Diurnal-Inertial Resonance: Numerical Experiments. Journal of Geophysical Research: Oceans 125. doi:10.1029/2020JC016208.

Franchito, S.H., Rao, V.B., Stech, J.L., Lorenzzetti, J.A., 1998. The effect of coastal upwelling on the sea-breeze circulation at Cabo Frio, Brazil: A numerical experiment. Annales Geophysicae 16, 866–866.

Gille, S.T., Lee, S.M., Llewellyn Smith, S.G., 2003. Measuring the sea breeze from QuikSCAT Scatterometry. Geophysical Research Letters 30. doi:10.1029/2002GL016230.

Gille, S.T., Llewellyn Smith, S.G., Statom, N.M., 2005. Global observations of the land breeze. Geophysical Research Letters 32. doi:10.1029/2004GL022139.

Graham, W.M., Largier, J.L., 1997. Upwelling shadows as nearshore retention sites: The example of northern Monterey Bay. Continental Shelf Research 17, 509–532. doi:10.1016/S0278-4343(96)00045-3.

Journal Pre-proof

Hyder, P., Simpson, J., Xing, J., Gille, S., 2011. Observations over an annual cycle and simulations of wind-forced oscillations near the critical latitude for diurnal–inertial resonance. Continental Shelf Research 31, 1576–1591. doi:10.1016/j.csr.2011.06.001.

Hyder, P., Simpson, J.H., Christopoulos, S., 2002. Sea-breeze forced diurnal surface currents in the Thermaikos Gulf, North-west Aegean. Continental Shelf Research 22, 585–601. doi:10.1016/S0278-4343(01)00080-2.

Jackett, D.R., Mcdougall, T.J., 1995. Minimal Adjustment of Hydrographic Profiles to Achieve Static Stability. Journal of Atmospheric and Oceanic Technology 12, 381–389. doi:10.1175/1520-0426(1995)012<0381:MAOHPT>2.0.CO;2.

Jarosz, E., Hallock, Z., Teague, W., 2007. Near-inertial currents in the DeSoto Canyon region. Continental Shelf Research 27, 2407–2426. doi:10.1016/j.csr.2007.06.014.

Kaplan, D.M., Largier, J.L., Navarrete, S., Guiñez, R., Castilla, J.C., 2003. Large diurnal temperature fluctuations in the nearshore water column. Estuarine, Coastal and Shelf Science 57, 385–398. doi:10.1016/S0272-7714(02)00363-3.

Kelly, S.M., 2019. Coastally Generated Near-Inertial Waves. Journal of Physical Oceanography 49, 2979–2995. doi:10.1175/JPO-D-18-0148.1.

Kundu, P.K., Chao, S.Y., McCreary, J.P., 1983. Transient coastal currents and inertio-gravity waves. Deep Sea Research Part A. Oceanographic Research Papers 30, 1059–1082. doi:10.1016/0198-0149(83)90061-4.

Lennard, C., Hahmann, A.N., Badger, J., Mortensen, N.G., Argent, B., 2015. Development of a Numerical Wind Atlas for South Africa. Energy Procedia 76, 128–137. doi:10.1016/j.egypro.2015.07.873.

Lucas, A.J., Pitcher, G.C., Probyn, T.A., Kudela, R.M., 2014. The influence of diurnal winds on phytoplankton dynamics in a coastal upwelling system off southwestern Africa. Deep Sea Research Part II: Topical Studies in Oceanography 101, 50–62. doi:10.1016/j.dsr2.2013.01.016.

Journal Pre-proof

Journal Pre-proof

Marchesiello, P., Debreu, L., Couvelard, X., 2009. Spurious diapycnal mixing in terrain-following coordinate models: The problem and a solution. Ocean Modelling 26, 156–169. doi:10.1016/j.ocemod.2008.09.004.

Meneghesso, C., Seabra, R., Broitman, B.R., Wethey, D.S., Burrows, M.T., Chan, B.K.K., Guy-Haim, T., Ribeiro, P.A., Rilov, G., Santos, A.M., Sousa, L.L., Lima, F.P., 2020. Remotely-sensed L4 SST underestimates the thermal fingerprint of coastal upwelling. Remote Sensing of Environment 237, 111588. doi:10.1016/j.rse.2019.111588.

Millot, C., Crépon, M., 1981. Inertial Oscillations on the Continentral Shelf aof the Gulf of Lions - Observations and Theory. Journal of Physical Oceanography 11, 639–657.

Nam, S., Send, U., 2013. Resonant Diurnal Oscillations and Mean Alongshore Flows Driven by Sea/Land Breeze Forcing in the Coastal Southern California Bight. Journal of Physical Oceanography 43, 616–630. doi:10.1175/JPO-D-11-0148.1.

Oliveira, P.B., Nolasco, R., Dubert, J., Moita, T., Peliz, Á., 2009. Surface temperature, chlorophyll and advection patterns during a summer upwelling event off central Portugal. Continental Shelf Research 29, 759–774. doi:10.1016/j.csr.2008.08.004.

Pettigrew, N.R., 1980. The Dynamics and Kinematics of the Coastal Boundary Layer off Long Island. Massachusetts Institute of Technology and Woods Hole Oceanographic Institution, Woods Hole, MA. doi:10.1575/1912/3727.

Pinkel, R., Goldin, M.A., Smith, J.A., Sun, O.M., Aja, A.A., Bui, M.N., Hughen, T., 2011. The Wirewalker: A Vertically Profiling Instrument Carrier Powered by Ocean Waves. Journal of Atmospheric and Oceanic Technology 28, 426–435. doi:10.1175/2010JTECHO805.1.

Pitcher, G., Figueiras, F., Hickey, B., Moita, M., 2010. The physical oceanography of upwelling systems and the development of harmful algal blooms. Progress in Oceanography 85, 5–32. doi:10.1016/j.pocean.2010.02.002.

Pollard, R., Millard, R., 1970. Comparison between observed and simulated wind-generated inertial oscillations. Deep Sea Research and Oceanographic Abstracts 17, 813–821. doi:10.1016/0011-7471(70)90043-4.

Journal Pre-proof

Pollard, R.T., 1980. Properties of Near-Surface Inertial Oscillations. Journal of Physical Oceanography 10, 385–398. doi:10.1175/1520-0485(1980)010<0385:PONSIO>2.0.CO;2.

Rainville, L., Pinkel, R., 2001. Wirewalker: An Autonomous Wave-Powered Vertical Profiler. Journal of Atmospheric and Oceanic Technology 18, 1048–1051. doi:10.1175/1520-0426(2001)018<1048:WAAWPV>2.0.CO;2.

Richter, I., 2015. Climate model biases in the eastern tropical oceans: Causes, impacts and ways forward. Wiley Interdisciplinary Reviews: Climate Change 6, 345–358.

Seroka, G., Fredj, E., Kohut, J., Dunk, R., Miles, T., Glenn, S., 2018. Sea Breeze Sensitivity to Coastal Upwelling and Synoptic Flow Using Lagrangian Methods. Journal of Geophysical Research: Atmospheres 123, 9443–9461. doi:10.1029/2018JD028940.

Shchepetkin, A.F., McWilliams, J.C., 2005. The regional oceanic modeling system (ROMS): A split-explicit, free-surface, topography-following-coordinate oceanic model. Ocean Modelling 9, 347–404. doi:10.1016/j.ocemod.2004.08.002.

Shearman, R.K., 2005. Observations of near-inertial current variability on the New England shelf. Journal of Geophysical Research: Oceans 110. doi:10.1029/2004JC002341.

Simpson, J.H., Hyder, P., Rippeth, T.P., Lucas, I.M., 2002. Forced Oscillations near the Critical Latitude for Diurnal-Inertial Resonance. Journal of Physical Oceanography 32, 177–187. doi:10.1175/1520-0485(2002)032<0177:FONTCL>2.0.CO;2.

Small, R.J., Curchitser, E., Hedstrom, K., Kauffman, B., Large, W.G., 2015. The Benguela upwelling system: Quantifying the sensitivity to resolution and coastal wind representation in a global climate model. Journal of Climate 28, 9409–9432.

Thomsen, S., Capet, X., Echevin, V., 2021. Competition between Baroclinic Instability and Ekman Transport under Varying Buoyancy Forcings in Upwelling Systems: An Idealized Analog to the Southern Ocean. Journal of Physical Oceanography 51, 3347–3364. doi:10.1175/JPO-D-20-0294.1.

Journal Pre-proof

Journal Pre-proof

Umlauf, L., Burchard, H., 2003. A generic length-scale equation for geophysical turbulence models. Journal of Marine Research 61, 235–265. doi:10.1357/002224003322005087.

Umlauf, L., Burchard, H., 2005. Second-order turbulence closure models for geophysical boundary layers. A review of recent work. Continental Shelf Research 25, 795–827. doi:10.1016/j.csr.2004.08.004.

Walter, R.K., Reid, E.C., Davis, K.A., Armenta, K.J., Merhoff, K., Nidzieko, N.J., 2017. Local diurnal wind-driven variability and upwelling in a small coastal embayment: Local wind-driven variability. Journal of Geophysical Research: Oceans 122, 955–972. doi:10.1002/2016JC012466.

Woodson, C.B., Eerkes-Medrano, D.I., Flores-Morales, A., Foley, M.M., Henkel, S.K., Hessing-Lewis, M., Jacinto, D., Needles, L., Nishizaki, M.T., O'Leary, J., Ostrander, C.E., Pespeni, M., Schwager, K.B., Tyburczy, J.A., Weersing, K.A., Kirincich, A.R., Barth, J.A., McManus, M.A., Washburn, L., 2007. Local diurnal upwelling driven by sea breezes in northern Monterey Bay. Continental Shelf Research 27, 2289–2302. doi:10.1016/j.csr.2007.05.014.

Xing, J., Davies, A.M., Fraunie, P., 2004. Model studies of near-inertial motion on the continental shelf off northeast Spain: A three-dimensional/two-dimensional/one-dimensional model comparison study. Journal of Geophysical Research: Oceans 109. doi:10.1029/2003JC001822.

Zhang, X., Smith, D.C., DiMarco, S.F., Hetland, R.D., 2010. A Numerical Study of Sea-Breeze-Driven Ocean Poincare Wave Propagation and Mixing near the Critical Latitude. Journal of Physical Oceanography 40, 48–66. doi:10.1175/2009JPO4216.1.

Journal Pre-proof

Journal Pre-proof

- Latitudinally dependent diurnal wind-driven internal waves enhance vertical mixing
- Vertical mixing drives surface layer retention and coastal warming during upwelling
- Diurnal wind-driven oscillations of the upwelling front explain observed temperatures
- Bottom slope steepness controls internal wave generation at the coast

Journal Pre-proof

Journal Pre-proof

Giles Fearon: Conceptualization, Methodology, Software, Formal analysis, Investigation, Writing - Original Draft, Visualization

Steven Herbette: Conceptualization, Methodology, Resources, Writing - Review & Editing, Supervision, Funding acquisition

Jennifer Veitch: Writing - Review & Editing, Supervision, Funding acquisition

Gildas Cambon: Software, Resources, Writing - Review & Editing

Marcello Vichi: Conceptualization, Methodology, Resources, Writing - Review & Editing, Supervision, Funding acquisition

Journal Pre-proof

Journal Pre-proof

Declaration of interests

☒ The authors declare that they have no known competing financial interests or personal relationships that could have appeared to influence the work reported in this paper.

☐The authors declare the following financial interests/personal relationships which may be considered as potential competing interests:

Journal Pre-proof